Scanning-laser glint measurements of sea-surface slope statistics

Joseph A. Shaw and James H. Churnside

A scanning-laser glint meter designed for field measurements of sea-surface slope statistics is described. A narrow laser beam is scanned in a line, and specular reflections (glints) are counted in bins according to their slope angle. From normalized glint histograms, moments to the fourth order are calculated, and slope probability density functions are approximated with a Gram–Charlier expansion. Field measurements with this instrument show good agreement with previous results when the stability (essentially air–sea temperature difference) is near neutral (zero). Under conditions of negative stability (warm ocean), both the mean-square slope and the probability density function kurtosis increase.

Key words: ocean optics, laser remote sensing, sea-surface roughness, atmospheric stability, statistical optics.

1. Introduction

The roughness of the ocean surface has a large influence on remote sensing measurements of surface and near-surface quantities. Remote measurements of near-surface winds,[1–3] sea-surface temperature,[4–7] ocean color,[8–10] and laser backscatter,[11–15] as well as imaging of underwater objects,[16] all depend to varying degrees on knowledge of sea-surface roughness. Short waves are the primary contributors to sea-surface slope and are strongly dependent on wind speed and air–sea temperature difference. These important short waves are best measured by optical slope techniques because of their steep slopes and small heights. In this paper we describe a new scanning-laser glint sensor and measurements taken with it of sea-surface slope statistics in the Pacific Ocean. This instrument measures slope probability density functions (PDF's) from normalized histograms of specular laser reflections (glints) in angle space. We use a Gram–Charlier series to compute PDF moments to the order of 4 and study the dependence of these moments on wind speed and stability of the air–sea interface (which is proportional to the air–sea temperature difference).

Published optical measurements of sea-surface slope statistics are not plentiful, partly because of the experimental difficulty involved in such measurements. The most complete field measurements of the slope PDF as a function of wind speed (1–14 m s^{-1}) are the classic sun-glitter photographs of Cox and Munk.[17,18] They related the density at each point in defocused sun-glitter photographs to the probability of occurrence for the wave slope corresponding to solar specular reflection. This technique worked well but required tedious data processing. Their measurements were made in the vicinity of the Hawaiian islands from an airplane at about a 600-m altitude during periods of neutral (equal air and water temperatures) and positive (air warmer than water) stability. Cox and Munk investigated the wind-speed but not the stability dependence of their data. They found a strong linear correlation of the mean-square slope, a weak correlation of the skewness, and no statistically significant correlation of the PDF kurtosis (peakedness relative to a Gaussian distribution) with wind speed.

After the work of Cox and Munk, there was a two-decade gap in field measurements until interest in ocean slope statistics was renewed by the deployment of scatterometers for near-surface wind sensing. Since that time most optical field measurements have been made with refractive laser slope gauges that determine local slopes from the refraction of light as it passes from an immersed laser source through the water–air interface to a receiver above the water.[19–22] These instruments enjoy large signal-to-noise ratios, but they require optics immersed in sea water and can disturb the surface.

Hughes *et al.*[23] used a refractive laser slope gauge

T. A. Shaw and J. H. Churnside are with the National Oceanic and Atmospheric Administration Environmental Technology Laboratory, 325 Broadway, Boulder, Colorado 80303.

Received 1 May 1996; revised manuscript received 12 February 1997.

to measure slope statistics in sheltered waters of the Bute Inlet and the Georgia Strait near Vancouver Island. They did not report air–sea temperature differences for each data point but did mention that the differences for the entire measurement period ranged from +1° to +10° C. Their data are in good agreement with those of Cox and Munk, showing a similar linear wind-speed dependence for the mean-square slope and a weak wind-speed dependence for skewness and kurtosis.

Tang and Shemdin's[24] measurements from a refractive laser slope gauge on a wave follower were the first that differed significantly from those of Cox and Munk. Some of their mean-square slope measurements, between wind speeds of 3 and 6 m s^{-1}, exceeded the Cox and Munk values by as much as a factor of 3. Because they did not measure the air–sea temperature difference, it is not possible to determine if negative stability was the cause. They found no significant wind-speed dependence for skewness and did not report any kurtosis results.

Haimbach and Wu[25] deployed a reflective scanning-laser system on a pier and found a linear wind-speed dependence of the mean-square slope similar to the Cox and Munk result. They commented that significant deviations appeared to follow the trends expected of stability. Those trends, as described for radar reflectivity,[26] are that positive stability suppresses ripples to produce smaller mean-square slopes, whereas negative stability enhances ripples to produce larger mean-square slopes. The mechanism, related to turbulence and convective exchange at the air–sea boundary,[26–28] is not completely understood.

Hwang and Shemdin[27] used a refractive laser slope gauge in the first ocean experiment to demonstrate the effects of stability and swell on optical slope measurements. After concluding that the effects of swell are much smaller than the effects of stability, they produced relationships for the amount of mean-square-slope suppression for a wide range of positive stability and showed evidence of mean-square-slope enhancement by negative stability. Wu[28] reanalyzed these data and showed the fundamental similarity of the effects of stability on optical and microwave (radar) measurements.

The measurements from our reflective laser-glint technique that we present in this paper extend the previous stability relationships for the mean-square slope deeper into the negative-stability regime. We find that mean-square slope increases with negative stability at roughly the same rate as it decreases with moderately positive stability. Our results agree well with the small amount of previously published negative-stability measurements, and they provide further evidence of the need for stability information when sea-surface slope measurements are interpreted. In our experiment the air–sea temperature difference was measured by a scanning millimeter-wave radiometer, which provides a differential measurement that results in less scatter in the data than do bulk temperature measurements.

Our measurements also show weak linear correlations of skewness and kurtosis with wind speed. Our results for the stability dependence of skewness and kurtosis are original: skewness is very weakly correlated with stability, whereas kurtosis is much more strongly correlated and tends to increase with negative stability (i.e., kurtosis depends on stability in a fashion similar to that of the mean-square slope). Finally, neither skewness nor kurtosis exhibit more than a weak correlation with the mean-square slope.

2. Laser-Glint-Meter Technique

A. Instrument Description

The laser-glint-meter technique develops slope statistics by counting laser glints from specular facets as a laser beam is scanned over the sea surface. Figure 1 illustrates the system layout, and Table 1 lists the primary system parameters. As indicated in Fig. 1, a 10-mW He–Ne laser beam (with a 1.18-mrad divergence) is directed by a spinning mirror onto the sea surface in a linear scan along an azimuth set by the user with a computer-controlled motor. The linear scan is oriented in any desired direction by a

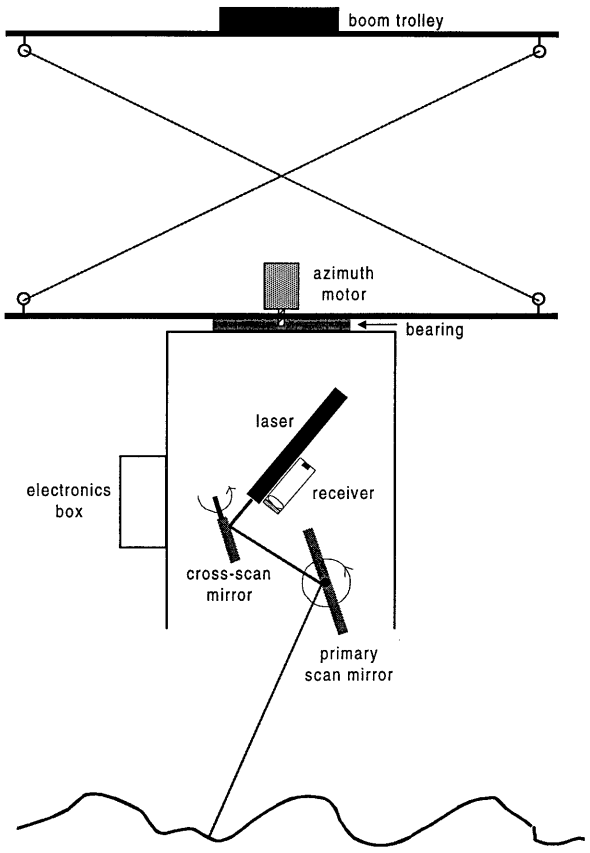

Fig. 1. Line drawing of the scanning-laser glint meter, showing the primary optical and mechanical components. The instrument is suspended from a boom with a system of two mounting plates connected with crossed aircraft cables; the azimuthal orientation of the optical package is set with a computer-controlled azimuth motor, which is bolted to the bottom mounting plate and coupled to the optics package with a 30-cm-diameter bearing.

Table 1. Summary of the Laser Glint Meter Hardware

Laser power	10 mW
Laser wavelength	632.8 nm
Laser far-field divergence	1.18 mrad
Laser polarization	Random
Detector	UDT 455 photodiode
Detector NEP at 1-kHz bandwidth	8×10^{-13} W
Entrance-pupil diameter	23 mm
Receiver optical filter bandwidth	10 nm
Receiver lens	F/4.3, 100-mm focus
Receiver optics transmittance (τ_O)	≈0.4
Receiver field of view	25.4 mrad
Mirror rotation rate	2 rev/s, adjustable
Glint sampling rate	0.1°/sample (nadir ± 75°)

computer-controlled motor that steers the optics package in azimuth. An intermediate cross-scan mirror is driven by another computer-controlled motor to compensate for cross-scan tilts caused by instrument motion. Instrument motion along the scan direction (caused by platform motion or wind-induced instrument motion) is compensated for by shifting of the angular bin locations at which glints from each scan are counted in the data-acquisition computer. Tilts in both axes are measured by inclinometers with a 2-Hz bandwidth.

The detector output is amplified with a remotely controlled gain, digitized at a rate of 0.1° per sample, and compared with a threshold value to classify each sample as "glint" or "no glint." Each scan covers a 150° range centered on nadir, and, to reduce data storage requirements, we record only the number of glints in each 1° bin. In our experiment the signal-to-noise ratio was high enough that a threshold could be set to discriminate glints clearly from background. Reflective markers (of roughly 1° angular extent) near the beginning and the end of the scan facilitate angular calibration to account for motor speed variations (≤5%) from scan to scan. Motor speed variations during a single scan produce errors that are smaller than the final 1° resolution of the glint histograms.

As the nadir angle increases, the laser-spot size at the surface grows larger. If the spot size were to become larger than the glint correlation length, the PDF would be biased high. From video images of laser glints,[29] we found this correlation length to be of the order of 10 cm at ~3-m s^{-1} wind speed, decreasing with increasing surface roughness. For the current data set the maximum nadir angle from which we recovered statistically significant slopes was ±45°, at which point the laser-spot size was 1.4 cm, comparable with the glint correlation length for the roughest surfaces observed. Therefore there is a possibility that the tails of our PDF's could be affected for the roughest surfaces we observed. However, the lack of a positive correlation between the wind speed and the kurtosis suggests that this is not a significant effect.

B. Radiometry

In this section we estimate the signal-to-noise ratio of the scanning-laser glint meter for a variety of sea-surface curvatures. The equations here are derived from geometrical optics and assume a specular, partially reflecting, anamorphic surface (see Appendix A). We assume that the surface has a maximum curvature κ_1 in the along-wind axis and a minimum curvature κ_2 in the crosswind axis (with $\kappa_2 = 0.25\ \kappa_1$).[30] The result is preferential spreading of the reflected laser beam in the along-wind axis, turning the originally circular laser beam into an elliptical one at the entrance-pupil plane. Concave and convex curvatures produce similar results because the curvature radii are much shorter than the range from the instrument to the surface.

A sufficient condition for validity of the anamorphic-mirror model is $k_w d_s \ll 1$, where k_w is the surface wave number and d_s is the laser-beam diameter at the surface. However, this condition is overly restrictive because the surface needs to conform to the model only over the very small region from which reflected light is actually collected by the receiver. In fact, light reaches the detector only from a small region of the surface around the specular point. For our receiver diameter and height, this is the region in which the slope is within 2 mrad of the specular point. This surface region is much smaller than the laser-spot size, especially for higher curvatures. Nevertheless, this model should not be applied to situations in which the laser spot can contain multiple glints; however, because our laser-spot diameter is generally smaller than the glint correlation length for the range of wind speeds and slopes encountered in this experiment, the anamorphic-mirror model provides a reasonable first-order estimate of the backscattered laser power for our instrument.

The resulting equation for the detected laser power, after reflection from the surface, is (see Appendix A for derivation)

$$P_d = \frac{\tau_0 R P_t D_{\mathrm{ep}}^{\ 2}}{\left(d_0 + \frac{\omega H}{\cos\theta}\right)^2 \left(1 + \frac{2\kappa_1 H}{\cos\theta}\right)\left(1 + \frac{2\kappa_2 H}{\cos\theta}\right)}. \quad (1)$$

In Eq. (1) τ_o is the optics transmittance, R is the surface reflectance, P_t is the transmitted laser power, D_{ep} is the optics entrance-pupil diameter, d_0 is the initial laser beam diameter, ω is the laser beam divergence angle, H is the instrument height above the surface, θ is the nadir angle at which the laser beam is pointed, and κ_1 and κ_2 are the along-wind and crosswind surface curvatures discussed above.

The detected background light is given by

$$P_b = \frac{\tau_O R E_{\lambda b} \Delta\lambda \pi D_d^{\ 2} D_{ep}^{\ 2}}{16 f^2}, \quad (2)$$

where $E_{\lambda b}$ is a uniformly distributed background spectral irradiance (in watts per square meter), $\Delta\lambda$ is the optical bandwidth of the receiver, D_d is the detector diameter, f is the receiver-lens focal length, and the other parameters are as defined above. The noise contribution of the background power depends on a modulation factor related to the surface rough-

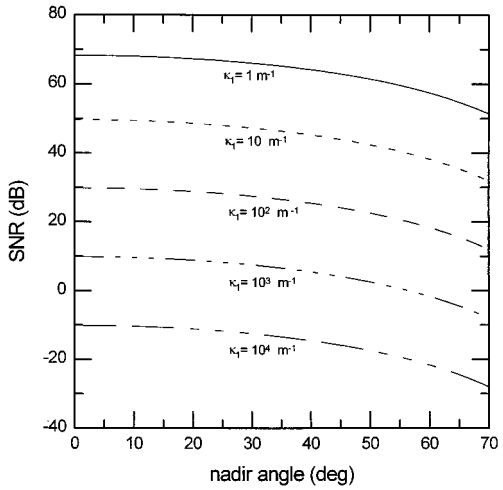

Fig. 2. Signal-to-noise ratio for the scanning-laser glint meter operating at 6 m above the surface at night. Each curve is for the annotated value of surface curvature.

ness. At night the background is low enough to be negligible for any modulation, whereas the daytime background dominates regardless of surface roughness. Therefore the nighttime signal-to-noise ratio is ten times the logarithm of the ratio of detected power to the receiver noise-equivalent power.

Figure 2 shows the signal-to-noise ratio estimated for nighttime operation with the parameters listed in Table 1 and $H = 6$ m, plotted as a function of nadir angle for various typical curvature values.[31] The weakest curvatures of $\kappa \approx 1\ \mathrm{m}^{-1}$ exist at very low wind speeds ($\leq 2\ \mathrm{m\ s}^{-1}$); $\kappa \approx 10\ \mathrm{m}^{-1}$ is expected for $\sim$2–3-m s^{-1} wind speeds; $\kappa \approx 10^2\ \mathrm{m}^{-1}$ is appropriate for $\sim$3–8-m s^{-1} wind speeds; $\kappa \approx 10^3\ \mathrm{m}^{-1}$ occurs for centimeter waves at $\sim$8–10-m s^{-1} wind speeds; and $\kappa \approx 10^4\ \mathrm{m}^{-1}$ represents extreme curvature, significant only in small capillary waves at wind speeds exceeding $\sim 10\ \mathrm{m\ s}^{-1}$. Thus the scanning-laser system can make nighttime measurements of centimeter waves with slopes as great as $\sim$45°. Daytime operation of the present system is impossible because direct or diffuse solar irradiance is stronger than a laser glint for nearly any combination of curvature and nadir angle. Both calculations and field experience show that moon glints are not a significant problem. We are currently in the process of designing a new system that will operate in daylight and perform full PDF scans in less time than the present system.

3. Experimental Conditions

The first field deployment of our system took place during the Coastal Ocean Probing Experiment near the Oregon coast in September 1995. The sensor was suspended from a boom on the Scripps Institution of Oceanography's Floating Instrument Platform (FLIP). The FLIP was moored 20 km from the Oregon coast, west of Tillamook, at coordinates 45° 45.22′ N latitude and 124° 16.9′ W longitude, in 150 m of water. All of our measurements were taken with the FLIP roughly 10 m downwind from our sensor to avoid contaminating the wind or wind-wave field. The height of the optics module was approximately 5–6 m above the surface.

For this deployment we designed a mounting system that would position the optics at a desired height of 5–6 m above the surface, allow the instrument to be brought in and out for adjustments, and minimize wind-induced instrument motion. This mount consisted of a 1-m square plate bolted to a boom trolley and another identical plate suspended $\sim$1.5 m below on aircraft cables crossed between corners of the upper and lower plates (see Fig. 1). The azimuth motor was mounted in the center of the lower plate with the optics package coupled to it with a 30-cm-diameter bearing. This arrangement successfully limited the total instrument motion, including wind-induced and FLIP motion, to less than ±4° at a rate slower than 2 Hz. The motion-compensating cross-scan mirror and along-scan bin adjustments described above successfully compensated for this remaining motion. The final angular uncertainty caused by instrument motion and motor speed variations is of the order of a PDF bin width (1°).

An ultrasonic range meter mounted on the optics package recorded the mean height above the surface for each scan. These data are useful for investigating the modulation of short waves by long waves (swell and internal waves). For the measurements reported here, the swell had periods of roughly 14 s, heights that varied between 1 and 3 m, and a direction of approximately 250° with respect to true north (80° west of the mean wind direction).

Winds were measured with a sonic anemometer mounted above the port boom at a height of 17 m. For standardization we adjusted these data to neutral 10-m-height wind speeds through the following equation, derived from a standard logarithmic profile[32]:

$$U_{10} = (u_*/0.4)\ln\left[\frac{10\exp(0.4U_{17}/u_*)}{17}\right], \qquad (3)$$

where U_{10} is the adjusted wind speed at 10 m, U_{17} is the wind speed measured at 17 m, and u_* is the friction velocity measured with the sonic anemometer as the covariance of the stream and vertical air velocities.[33] For the data discussed here, wind speeds varied from approximately 4 to 10 m s^{-1} with a direction of approximately 170° ± 20°.

To characterize the stability of the air–sea interface, we measured air–sea temperature differences with an elevation-scanning millimeter-wave radiometer.[34] This radiometer uses the high absorption of the 60-GHz (5-mm wavelength) O_2 band to measure the air temperature in the vicinity of the radiometer and the air–sea temperature difference with a penetration depth in the water of approximately 0.3 mm. The principal advantages of this technique are that it measures the important skin temperature, which is intimately connected with the air–sea interaction,[35] and it provides a differential measurement that has

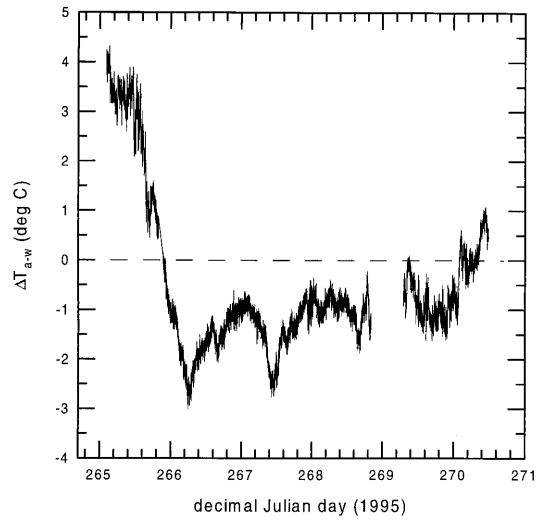

Fig. 3. Air–water temperature difference measured by an elevation-scanning millimeter-wave radiometer on the FLIP port boom. Positive values correspond to positive stability, and negative values correspond to negative stability.

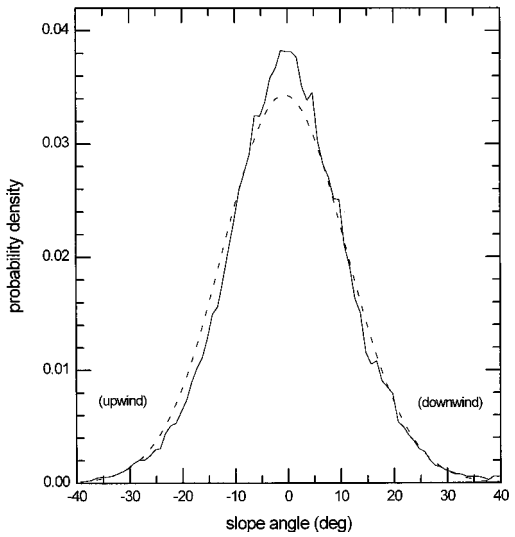

Fig. 4. Measured along-wind slope PDF (solid curve) and a Gaussian distribution with the same mean and variance (dashed curve). The skewness toward downwind slopes caused by wave asymmetry is evident.

higher accuracy and stability than two independent bulk or radiometric sensors can provide. Figure 3 shows a plot of the 5-mm radiometer air–sea temperature difference measurements for the period under consideration here (primarily Julian days 268–270, or September 25–27, 1995).

The parameter we use to represent stability is a reduced Richardson number, given by

$$\mathrm{Ri} = g\Delta T_{a-w} z / T_w U_z^2, \tag{4}$$

where g is gravitational acceleration (9.8 m s^{-2}), ΔT_{a-w} is the air–sea temperature difference (degrees Centigrade), U_z is the mean wind speed (in meters per second) measured at height z (10 m), and T_w is the mean water temperature (degrees Centigrade). Ri is positive for stable conditions (air warmer than water), zero for neutral cases (equal air and water temperatures), and negative for unstable cases (air colder than water).

4. Slope Probability Density Functions

Figure 4 shows a typical along-wind slope PDF (solid curve) from a 20-min measurement (2200 scans), plotted as a function of slope angle with respect to nadir; positive slopes are downwind and negative slopes are upwind. Also shown is a Gaussian distribution (dashed curve) with the same mean and variance. Despite the general Gaussian appearance of the measured PDF, significant deviations from the Gaussian are apparent. These differences, which carry important information about the surface roughness, can be described by coefficients of skewness and kurtosis. Because wind-driven waves are asymmetric, tending to lean downwind, the scanning laser encounters more large-angle glints when pointed at the steeper downwind faces of the waves. This results in a net negative skewness in the along-wind PDF toward downwind slopes in comparison with a symmetrical Gaussian. No significant skewness occurs in the crosswind PDF because there is no wind-driven asymmetry. Unfortunately, because operational difficulties greatly limited the number of crosswind measurements, we must limit subsequent discussion to along-wind PDF's.

In an approach similar to that of Cox and Munk,[17,18] we computed a Gram–Charlier series[36,37] to obtain an analytical estimate of each measured PDF. To simplify the polynomials, we expanded the PDFs in terms of a normalized slope,

$$\eta = (\theta - \bar{\theta})/\sigma, \tag{5}$$

where θ is the slope angle with respect to nadir, $\bar{\theta}$ is the mean slope angle, and σ is the measured PDF standard deviation. The series representation of the slope probability density function is then

$$p(\eta) = \sum_{n=0}^{N} (c_n/n!) H_n(\eta) G(\eta), \tag{6}$$

where $G(\eta)$ is a zero-mean, unit-variance Gaussian distribution,

$$G(\eta) = (1/\sqrt{2\pi}) \exp(-\eta^2/2), \tag{7}$$

$H_n(\eta)$ are the nth-order Hermite polynomials[36,37] listed in Table 2, and c_n are the expansion coefficients computed by the following summation of the measured slope-PDF values:

$$c_n = \sum_j \mathrm{PDF}(\eta_j) H_n(\eta_j). \tag{8}$$

Given that $H_0 = 1$ and that $c_1 = c_2 = 0$ because we have already matched the mean and variance to the experimental data, Eq. (6) takes the form of a summation of a best-fit Gaussian plus higher-order terms that

Table 2. Hermite Polynomials of Order n

n	$H_n(\eta)$
0	1
1	η
2	$\eta^2 - 1$
3	$\eta^3 - 3\eta$
4	$\eta^4 - 6\eta^2 + 3$
5	$\eta^5 - 10\eta^3 + 15\eta$
6	$\eta^6 - 15\eta^4 + 45\eta^2 - 15$
7	$\eta^7 - 21\eta^5 + 105\eta^3 - 105\eta$
8	$\eta^8 - 28\eta^6 + 210\eta^4 - 420\eta^2 + 105$

correct for skewness and kurtosis (odd terms are related to skewness; even terms are related to kurtosis).

Extraneous features on the PDF's were sometimes caused by breaking waves, interfering background light, sea gulls flying or floating through the beam, sea lion heads, or mooring lines blocking part of the beam (when the platform was occasionally rotated by strong winds from the south). Especially when these features occur in the tails of the PDF (as they usually do), the mean-square slope may be determined adequately but the higher-order moments are not. In these cases the Gram–Charlier representation did not converge, and such measurements have been eliminated from this analysis.

Figure 5 shows one of the well-behaved Gram–Charlier PDF expansions for which the normalized error is shown in Fig. 6. This error is the difference between the estimated and the measured PDF's, divided point-by-point by the measurement uncertainty of each PDF bin. By Poisson statistics, the latter uncertainty is simply the square root of the number of glints counted in that bin normalized by the total number of counts in the histogram. Thus a normalized error with a magnitude of the order of 1 means that the residual differences between the measured and estimated PDFs are of the order of the statistical noise in the PDF measurement, and therefore further terms in the series are insignificant. The normalized error in Fig. 6 shows outstanding convergence, with nearly the entire angular range of the PDF estimated by the Gram–Charlier expansion to within one standard deviation of the glint-count process. The series-expansion for the estimated PDF, shown in Fig. 5, includes terms as high as $n = 8$, but roughly 90% of the correction is contained within the $n = 3$ and $n = 4$ terms. Recall that these are the first nonzero correction terms (i.e., $c_1 = c_2 = 0$) because the mean and the variance were fixed to match the measured PDF. We find that, for nearly all well-behaved measurements, expansion to $n = 4$ brings the normalized error to within 2–4 glint-count standard deviations; $n = 6$, to within 2–3 glint-count standard deviations; and $n = 8$, to within 1–2 glint-count standard deviations. Further terms carry no statistically significant information.

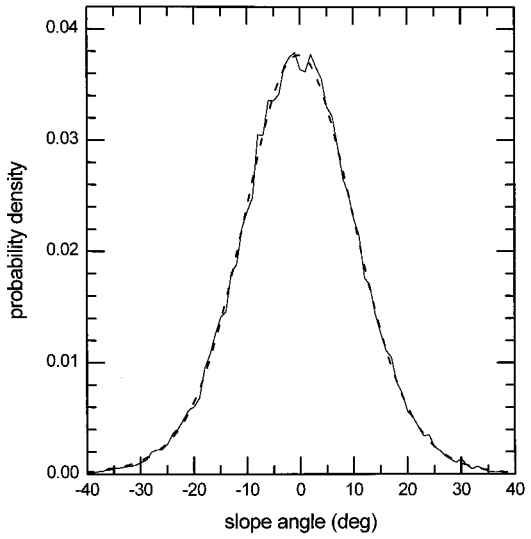

Fig. 5. Measured along-wind slope PDF (solid curve) and the corresponding PDF calculated with a Gram–Charlier series (dashed curve).

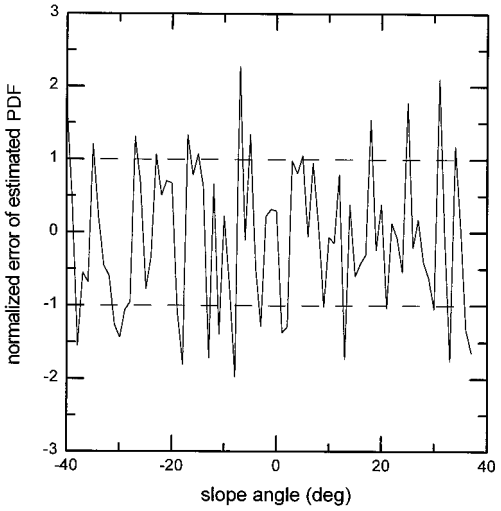

Fig. 6. Normalized error of the estimated PDF in Fig. 5, equal to the difference between the measured and estimated PDF values divided by the statistical uncertainty of the measured PDF. A normalized error of ± 1 or less means that the Gram–Charlier series estimates the measured PDF to within the statistical uncertainty of the measurement.

Because they contain nearly the complete correction, we use the third- and fourth-order Gram–Charlier series coefficients (c_3 and c_4) to represent skewness and kurtosis, respectively. Owing to the form of the Hermite polynomials, c_3 is a scaled third central moment and c_4 is a scaled fourth central moment of the PDF. The scaling is exactly that required for computing the usual coefficients[38] of skewness,

$$c_3 = m_3/\sqrt{m_2^3}, \tag{9}$$

and kurtosis,

$$c_4 = m_4/m_2^2, \tag{10}$$

Table 3. Scanning-Laser Data Summary[a]

Julian day 1995	Start Time (UTC)	U_{10} ($m\ s^{-1}$)	u_* ($m\ s^{-1}$)	ΔT_{a-w} (°C)	T_w (°C)	σ_a^2	c_3	γ
268	0754	5.76	0.21	−0.904	17.06	0.039	1.967	
	0814	5.54	0.19	−0.951	17.00	0.035	2.117	
	0834	5.20	0.18	−0.969	16.99	0.032	−0.022	1.885
	0854	5.11	0.16	−0.929	16.99	0.031	−0.151	2.075
	0914	4.69	0.15	−0.809	16.96	0.029	−0.027	2.464
	0934	4.91	0.12	−0.848	16.94	0.031	−0.005	2.028
	0954	5.05	0.18	−0.827	16.92	0.031	−0.063	1.884
	1014	4.71	0.22	−0.851	16.92	0.031	0.012	2.395
	1034	4.85	0.21	−0.878	16.91	0.034	−0.079	2.575
	1054	5.31	0.20	−0.817	16.95	0.025	−0.131	1.334
269	0246	4.03	0.23		17.41	0.025	−0.017	0.752
	0306	4.38	0.26		17.37	0.024	−0.014	0.786
	0326	4.68	0.28		17.39	0.023	−0.003	0.868
	0346	4.04	0.24		17.39	0.030	0.121	1.317
	0403	4.91	0.20		17.34	0.024	−0.033	0.778
	0423	5.19	0.20		17.31	0.025	−0.244	1.110
	0443	5.13	0.16		17.28	0.024	−0.084	0.711
	0503	5.14	0.12		17.29	0.024	−0.129	1.215
	0518	5.38	0.15		17.28	0.031	−0.154	1.689
	0538	5.99	0.17		17.24	0.030	−0.206	1.544
	0558	6.44	0.10		17.20	0.029	−0.019	1.022
	0618	5.99	0.09		17.19	0.028	−0.148	1.113
	0638	5.63	0.14		17.12	0.029	−0.159	0.986
	0646	5.68	0.17		17.12	0.030		1.190
	0706	5.03	0.34	−0.581	17.08	0.029	−0.053	1.326
	0726	4.66	0.51	−0.559	17.05	0.027	0.021	1.094
	0742	4.87	0.45	−0.820	17.08	0.029	−0.215	1.688
	0802	4.42	0.23	−0.595	17.10	0.031	−0.121	1.373
	0822	4.63	0.17	−0.180	17.09	0.026	−0.250	1.230
	0848	4.51	0.20	−0.098	17.07	0.018		
	0908	4.99	0.20	−0.215	17.06	0.027	−0.023	1.339
	0928	5.51	0.25	−0.343	17.09	0.028	−0.190	2.113
	0959	6.46	0.25	−0.415	17.12	0.028	−0.079	1.092
	1019	6.17	0.27	−0.491	17.12	0.031	−0.188	1.130
	1039	5.9	0.23	−0.473	16.99	0.032	−0.342	1.280
	1102	7.47	0.08	−0.757	17.02	0.039	−0.139	1.29
	1122	7.87	0.14	−0.833	17.02	0.037	−0.088	0.761
	1142	8.76	0.30	−0.871	16.99	0.038	−0.030	0.717
	1202	8.61	0.27	−0.864	17.01	0.043	−0.150	0.980
	1222	8.59	0.31	−1.036	16.92	0.038	−0.035	0.369
	1242	8.74	0.29	−1.065	16.91	0.042	−0.186	0.846
	1308	9.37	0.28	−1.120	17.00	0.046	−0.156	1.092
270	0545	7.28	0.33	−0.045	16.14	0.034		
	0648	8.38	0.34	−0.113	16.54	0.035		
	0708	8.22	0.33	−0.0063	16.53	0.046		2.225
	0916	8.23	0.27	0.634	15.41	0.023		
	1102	8.84	0.30	0.661	15.46	0.028		
	1122	9.01	0.28	0.535	15.53	0.029		
	1142	9.05	0.32	0.528	15.58	0.031		2.002

[a]Blanks indicate no available data.

where m_x represents the xth-order central moment. Because $c_4 = 3$ for a Gaussian distribution, we represent the kurtosis with respect to a Gaussian distribution by the coefficient of excess,[38]

$$\gamma = c_4 - 3. \tag{11}$$

These coefficients, c_3 and γ, as well as the along-wind mean-square slopes σ_a^2, are listed along with the corresponding wind-speed and stability data in Table 3.

5. Moments of the Slope Probability Density Function

A. Mean-Square Slope

Figure 7 shows our measured along-wind mean-square slopes as a function of U_{10}. Statistical measurement fluctuations are within the size of the symbols on the plot; the dominant uncertainty is the

5–15% standard deviation of the wind speed over the 20-min measurement time. In Fig. 7 the squares correspond to near-neutral stability, and the dots correspond to negative stability (air–sea temperature difference between −0.1 and −1.1 °C). The dashed line is the Cox and Munk linear regression for the along-wind, clean-surface mean-square slope, measured under conditions of near-neutral stability; the solid line is a linear regression through our negative-stability data. Our few data points taken during near-neutral stability agree with the Cox and Munk regression, demonstrating the essential validity of our technique. The more numerous points taken under negative stability are significantly higher than the Cox and Munk regression.

Figure 8 shows the wind-speed dependence of the along-wind mean-square slopes measured by several techniques. Data from our laser glint meter are shown as dots, data from Hwang and Shemdin's[27] refractive laser slope gauge are shown as crosses, and data from Cox and Munk's[17,18] sun-glitter photographs are shown as triangles. The increased scatter in both of the later data sets over the Cox and Munk data is caused largely by wider ranges of stability. This is illustrated in Figs. 9–10, which show plots of the ratio of the along-wind mean-square slope σ_a^2 to the Cox and Munk along-wind mean-square slope σ_{cm}^2 versus the stability of the air–sea interface.

Figure 9 shows a plot of the normalized mean-square slope σ_a^2/σ_{cm}^2 versus the Richardson number (σ_a^2 is our along-wind mean-square slope measurement, and σ_{cm}^2 is the corresponding Cox and Munk linear regression value for the clean-surface, along-wind mean-square slope). The trend of increasing mean-square slope with increasing negative stability is clear. The linear regression shown as a solid line in Fig. 9 (with a linear correlation coefficient of $r = 0.87$) is given by

$$\sigma_a^2/\sigma_{cm}^2 = 1.31 - 3.54\ \mathrm{Ri}, \qquad -0.23 \le \mathrm{Ri} \le 0.060. \tag{12}$$

In Fig. 10 our data are combined with Hwang and Shemdin's[27] data in a similar plot versus the Richardson number. This figure demonstrates the similarity but opposite sign of the effect that moderately positive and negative stability have on mean-square slope. For strong positive stability the mean-square-slope suppression becomes roughly constant; such a saturation effect for negative stability was not observed within the range of our measurements.

The solid lines in Fig. 10 represent approximate best-fit lines that describe the ratio of the normalized

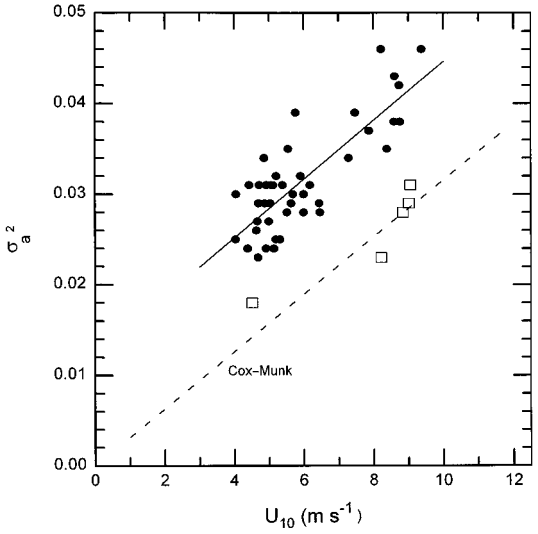

Fig. 7. Wind-speed dependence of the along-wind mean-square slope measured by the scanning-laser glint meter for negative stability (dots) and near-neutral stability (boxes). The dashed line is the Cox and Munk along-wind mean-square slope regression line; the solid line is a regression through our data.

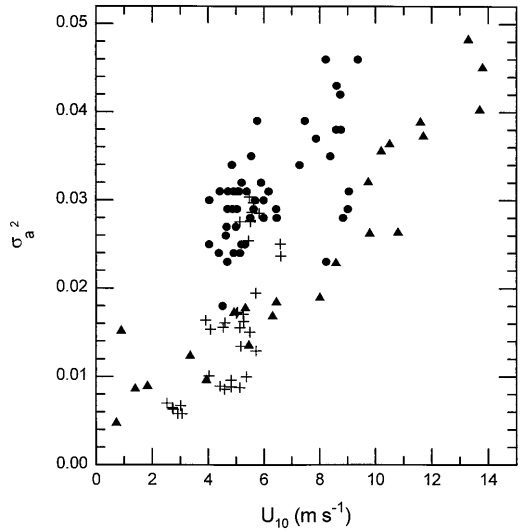

Fig. 8. Wind-speed dependence of the along-wind mean-square slope measured by our scanning-laser glint meter (dots), Hwang and Shemdin's refractive laser slope gauge (crosses), and Cox and Munk's sun-glitter photographs (solid triangles).

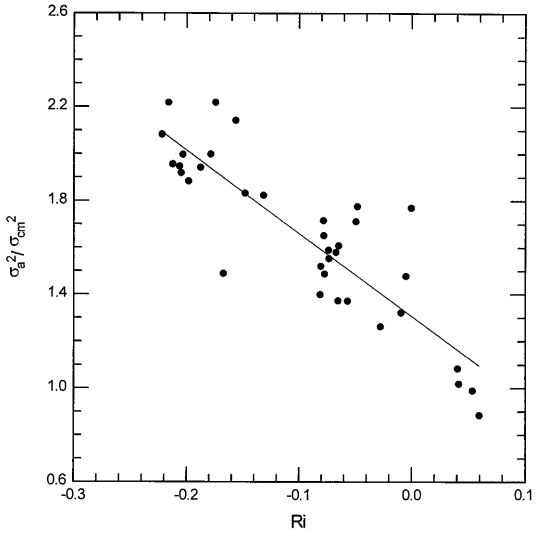

Fig. 9. Stability dependence of the normalized along-wind mean-square slope measured by our scanning-laser glint meter.

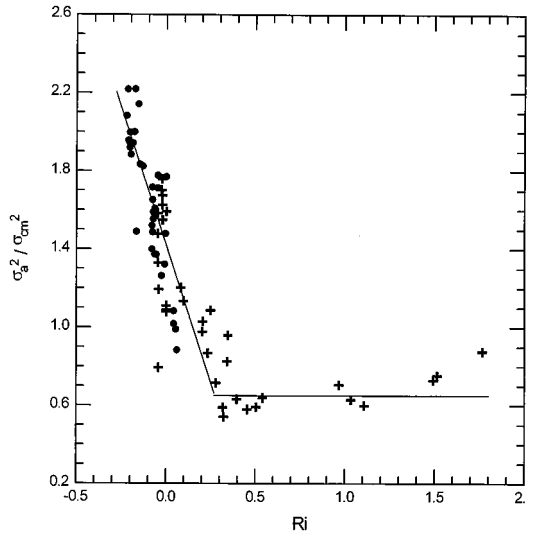

Fig. 10. Stability dependence of the normalized along-wind mean-square slope measured by our scanning-laser glint meter (dots) and Hwang and Shemdin's refractive laser slope gauge (crosses).

mean-square slope as a function of stability. The corresponding equations are

$$\sigma_a^2/\sigma_{cm}^2 = 1.42 - 2.80\ \mathrm{Ri}, \quad -0.23 < \mathrm{Ri} < 0.27, \tag{13}$$

$$\sigma_a^2/\sigma_{cm}^2 = 0.65, \qquad \mathrm{Ri} \geq 0.27. \tag{14}$$

Inclusion of Hwang and Shemdin's data results in a slightly larger intercept and a moderately smaller slope than are obtained from our data alone. The right-hand side of Eq. (13) has a value larger than unity at neutral stability (Ri = 0) because the Cox and Munk data were collected under primarily positive stability, so they represent smaller values of the mean-square slope than a neutral-stability case. In fact, after removing two curiously large values, we find that the remaining clean-surface Cox and Munk measurements yield an average value of 0.17 for Ri. Agreeing within the experimental uncertainty of this value, Eq. (13) is unity when Ri = 0.15.

B. Skewness

Figure 11 shows the wind-speed dependence of the coefficient of skewness, c_3, for along-wind measurements. The plotted data are limited to points for which the higher-order moments are well behaved, as discussed above. More of the measurements at high wind speeds had unstable higher moments than those at low wind speeds. This suggests that we could be detecting extraneous large-angle glints from breaking waves at higher wind speeds. The edited data cluster in the 4–6-m s^{-1} wind-speed range, with only a few points at higher wind speeds. All but three of the data points have a negative skewness, as expected from the wave asymmetry discussed earlier, but there is a wide scatter in the data plotted versus the wind speed. The resulting linear regression of c_3 with wind speed is

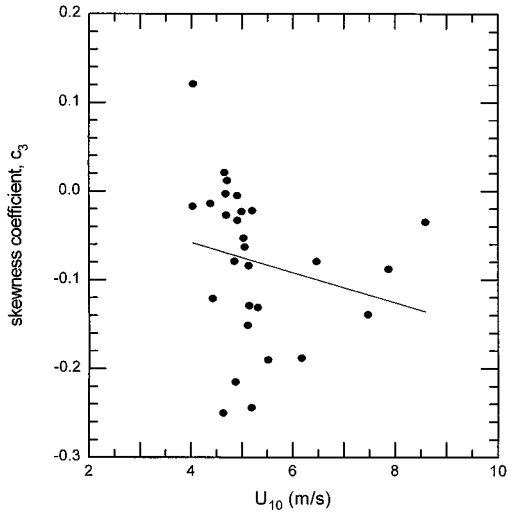

Fig. 11. The PDF skewness exhibits only weak linear correlation with wind speed.

$$c_3 = 0.0101 - 0.0170U_{10} \pm 0.087 \qquad (r = -0.21). \tag{15}$$

The small value of r, the intercept standard error of 0.0830, and especially the slope standard error of 0.0154 show that this trend is statistically very weak but still significant, which is similar to the Cox and Munk result.

We found a similar result for the stability dependence of skewness, shown in Fig. 12. This figure contains fewer data points than Fig. 11 because air–sea temperature differences were not available for every PDF. Again, a wide scatter exists in the data, but a statistically significant trend does exist (the standard errors are 0.0413 for the intercept and 0.273 for the slope):

$$c_3 = -0.124 - 0.281\ \mathrm{Ri} \pm 0.081 \qquad (r = 0.23). \tag{16}$$

Without assigning excessive value to these weak statistical correlations, we believe it is fair to say that stability is at least as important as wind speed in determining the value of skewness, but neither effect is clearly dominant in our measurements.

C. Kurtosis

The kurtosis γ also exhibits very weak correlation with wind speed, as shown in Fig. 13. Kurtosis tends to be reduced by increased wind speed, according to the linear regression shown in Fig. 13 (with standard errors of 0.339 for the intercept and 0.0559 for the slope), which is given by

$$\gamma = 1.880 - 0.0834U_{10} \pm 0.543 \qquad (r = 0.23). \tag{17}$$

A much more significant correlation exists between kurtosis and stability, as shown in Fig. 14. The linear regression, shown as a solid line, is given by

$$\gamma = 0.463 - 7.643\ \mathrm{Ri} \pm 0.328 \qquad (r = 0.83). \tag{18}$$

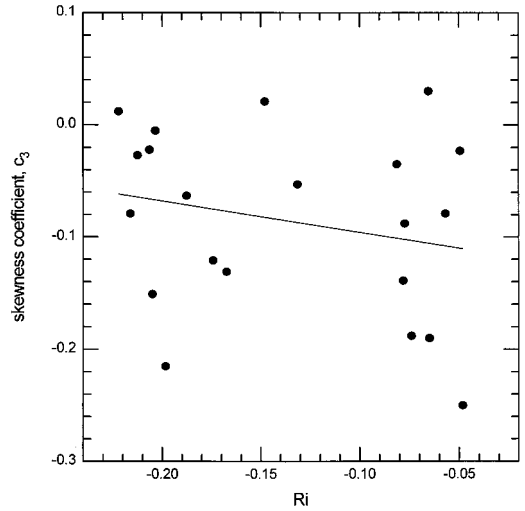

Fig. 12. The PDF skewness is only weakly correlated with the stability of the air–sea interface.

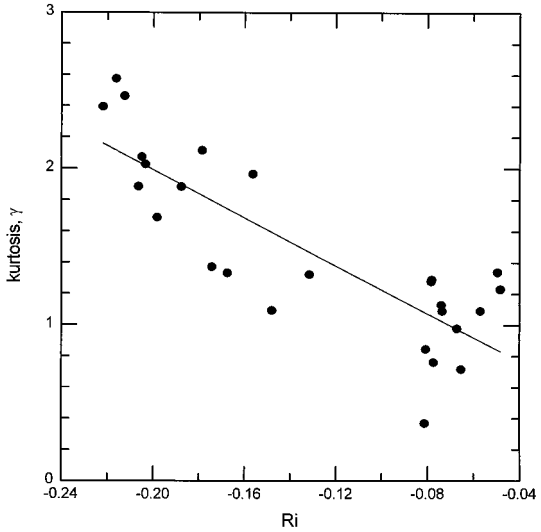

Fig. 14. The PDF kurtosis is significantly correlated with the stability of the air–sea interface.

The standard errors of the regression intercept and slope, respectively, are 0.152 and 1.037 for Eq. (18). It is clear from Fig. 14 that stability must be considered for adequate definition of kurtosis in a sea-surface slope PDF.

It is interesting that the neutral-stability intercept of Eq. (18) is $\gamma = 0.46 \pm 0.33$, which is statistically equivalent to the Cox and Munk coefficient, $c_{04} = 0.23 \pm 0.41$ (found to be independent of wind speed but not analyzed as a function of stability). Recognizing that the Cox and Munk measurements were made under near-neutral (but slightly positive) stability, we propose that the Cox and Munk result is actually an average kurtosis value for near-neutral stability. It is interesting to see what the kurtosis looks like as a function of positive stability in future data.

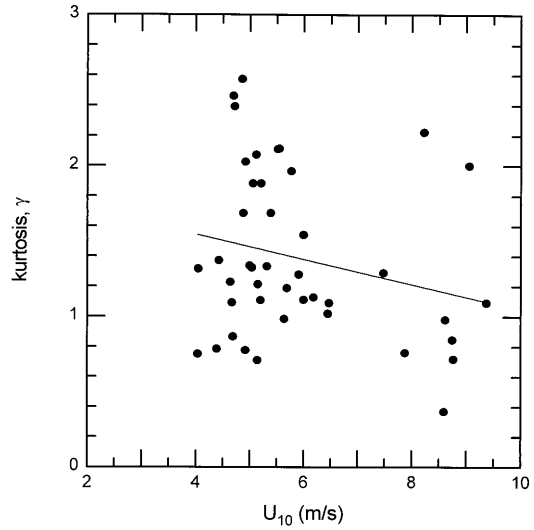

Fig. 13. The PDF kurtosis exhibits only weak correlation with wind speed.

6. Discussion

Given that the mean-square slope depends on both wind speed and stability, it is reasonable to ask whether or not skewness or kurtosis can be determined by the mean-square slope alone. Theoretical work by Longuet–Higgins[39] suggested that the skewness might be predictable from the mean-square slope. However, the same paper points out that the predicted dependency did not exist in the Cox and Munk data and that therefore the theory did not apply to those observations. Our results are in agreement with this assessment, for we find only weak correlation of skewness or kurtosis with the mean-square slope. The linear regression for the skewness versus the mean-square slope (with standard errors of 0.139 for the intercept and 4.446 for the slope) is given by

$$c_3 = -0.2349 + 4.812\ \sigma_a^{\,2} \pm 0.0809 \qquad (r = 0.24), \tag{19}$$

and the linear regression for kurtosis versus the mean-square slope (with standard errors of 0.6818 for the intercept and 20.31 for the slope) is given by

$$\gamma = 2.505 - 31.12\ \sigma_a^{\,2} \pm 0.566 \qquad (r = 0.29). \tag{20}$$

Since the mean-square slope alone is not sufficient for determining skewness or kurtosis, it is possible that there is yet another important physical parameter.

7. Conclusions

We have described a new reflective scanning-laser glint sensor for measuring sea-surface slope statistics. This system can measure a large range of slopes and is relatively simple to construct and operate. Measurements taken with this instrument in the Pacific Ocean agree well with previous measurements made under similar stability conditions. These data are, to our knowledge, the first published

optical field measurements from the open ocean of mean-square-slope enhancement by this large a range of negative stability, and they are the first measurements of slope-PDF skewness and kurtosis as a function of stability. The results show that skewness is only weakly correlated with stability but that kurtosis is strongly correlated. The behavior of kurtosis with stability is similar to that of the mean-square slope, having a greater magnitude for increasingly negative stability. Finally, neither skewness nor kurtosis can be determined sufficiently by the mean-square slope alone. The utility of this technique in studies of ocean-surface phenomena is evident, especially in combination with a differential radiometric measurement of air–sea temperature difference.

Appendix A: Derivation of Detected-Power Equations

This appendix contains the derivation of Eqs. (1) and (2). These equations are derived from geometrical optics to describe the first-order signal-to-noise performance of a laser-glint sensor. The model treats specular ocean-surface facets as anamorphic mirrors in the plane transverse to the optical (propagation) axis, so that each facet has maximum curvature κ_1 in the along-wind axis and minimum curvature κ_2 in the crosswind axis of the transverse plane. We assume that $\kappa_2 = 0.25\ \kappa_1$, in accordance with the wave-number-independent form of the wave-spectrum azimuthal variation.[30] This derivation traces the laser beam from its source, via a specular reflection at an anamorphic surface facet, back through the receiver optics to the detector.

The transmitted laser beam has an initial diameter d_0 and a far-field divergence angle ω. So when the laser is pointed at nadir angle θ from height H, the laser-spot diameter at a normally oriented surface facet is equal to

$$d = d_0 + \omega H/\cos\theta. \tag{A1}$$

A single optical ray at the edge of the laser beam intersects the surface at a transverse distance of $d/2$ from the optical axis. The reflection angle u' (with respect to the optical axis) depends on the surface curvature and is given by

$$u' = d\kappa. \tag{A2}$$

When the reflected ray arrives back at the entrance-pupil plane, its displacement from the optical axis is given by

$$r' = d(1/2 + \kappa H/\cos\theta). \tag{A3}$$

The reflected light beam is elliptical when it reaches the entrance-pupil plane because of the two different surface curvatures. With the orthogonal beam diameters represented by d_1 and d_2, the irradiance of the reflected laser beam at the entrance-pupil plane is

$$E_r = 4RP_{\text{laser}}/\pi d_1 d_2, \tag{A4}$$

where R is the surface reflectance. (We use $R = 0.02$ for the air–water interface.) The power detected by the receiver, P_d, is equal to the irradiance in Eq. (A4) multiplied by the entrance-pupil area (D_{ep} is the entrance-pupil diameter) and the optics transmittance τ_o:

$$P_d = E_r\tau_O\frac{\pi D_{\text{ep}}{}^2}{4} = \frac{\tau_O R P_{\text{laser}} D_{\text{ep}}{}^2}{d_1 d_2}. \tag{A5}$$

We express this equation in terms of more fundamental parameters by replacing both d_1 and d_2 with $2r'$ from Eq. (A3), using κ_1 and κ_2, respectively, and using (A3) to rewrite d. The resulting equation for detected laser power is given as Eq. (1).

When calculating the background light for uniform background radiance $L_{\lambda b}$, we can ignore the surface curvature because the same background is reflected into the field of view by waves of all slopes. Thus the diffuse-background power detected in a solid angle Ω_d through the entrance-pupil area A_{ep} with a spectral bandwidth $\Delta\lambda$ is

$$P_b = \tau_O R L_{\lambda b}\Delta\lambda A_{\text{ep}}\Omega_d. \tag{A6}$$

Expressing A_{ep} and Ω_d in terms of receiver parameters and writing the radiance in terms of irradiance ($L_{\lambda b} = E_{\lambda b}/\pi$) converts Eq. (A6) into Eq. (2).

This document was generated as part of the joint National Oceanic and Atmospheric Administration and Department of Defense Advanced Sensor Applications Program. We thank Mark Jacobson for help in collecting data on the FLIP, James Wilczak and Chris Fairall for the wind measurements and helpful discussions about stability, Yuri Trokhimovski for the 5-mm radiometer data, and the reviewers for their helpful suggestions.

References

1. A. K. Fung, *Microwave Scattering and Emission Models and Their Applications* (Artech House, Boston, Mass., 1994).
2. S. H. Yueh, W. J. Wilson, F. K. Li, S. V. Nghiem, and W. B. Ricketts, "Polarimetric measurements of sea surface brightness temperatures using an aircraft K-band radiometer," IEEE Trans. Geosci. Remote Sens. **33**(1), 85–92 (1995).
3. Y. G. Trokhimovski and V. G. Irisov, "Wind speed and direction measurement using microwave polarimetric radiometers," *NOAA Technical Memo ERL ETL-250* (National Technical Information Service, 5285 Port Royal Road, Springfield, Va. 22161, 1995).
4. A. P. Cracknell, "A method for the correction of sea surface temperatures derived from satellite thermal infrared data in an area of sunglint," Int. J. Remote Sens. **14**(1), 3–8 (1993).
5. K. Yoshimori, K. Itoh, and Y. Ichioka, "Thermal radiative and reflective characteristics of a wind-roughened water surface," J. Opt. Soc. Am. A **11**(6), 1886–1893 (1994).
6. K. Yoshimori, K. Itoh, and Y. Ichioka, "Statistically corrected ocean thermography," Appl. Opt. **33**(30), 7078–7087 (1994).
7. K. Yoshimori, K. Itoh, and Y. Ichioka, "Optical characteristics of a wind-roughened water surface: a two-dimensional theory," Appl. Opt. **34**(27), 6236–6247 (1995).

8. H. R. Gordon and M. Wang, "Surface-roughness considerations for atmospheric correction of ocean color sensors. I: the Rayleigh-scattering component," Appl. Opt. **31**(21), 4247–4260 (1992).
9. H. R. Gordon and M. Wang, "Surface-roughness considerations for atmospheric correction of ocean color sensors. II: error in the retrieved water-leaving radiance," Appl. Opt. **31**(21), 4261–4267 (1992).
10. H. R. Gordon and M. Wang, "Retrieval of water-leaving radiance and aerosol optical thickness over the oceans with SeaWiFS: a preliminary algorithm," Appl. Opt. **33**(3), 443–452 (1994).
11. G. L. Stamm and L. A. Harris, "Sea echo measurements made with 1.06-μm laser radiation," Appl. Opt. **13**(11), 2477–2479 (1974).
12. J. L. Bufton, F. E. Hoge, and R. N. Swift, "Airborne measurements of laser backscatter from the ocean surface," Appl. Opt. **22**(17), 2603–2618 (1983).
13. J. A. Reagan and D. A. Zielinskie, "Spaceborne lidar remote sensing techniques aided by surface returns," Opt. Eng. **30**(1), 96–102 (1991).
14. T. W. Cooley and J. A. Reagan, "Calibration of 1064 nm channel of LITE and other uses of ocean surface returns," in *IGARSS '93, Tokyo, 18–21 August 1993* (IEEE, New York, 1993), pp. 869–871.
15. D. M. Winker, R. H. Couch, and P. M. McCormick, "An overview of LITE: NASA's Lidar In-space Technology Experiment," IEEE Proc. **84**(2), 164–180 (1996).
16. J. W. McLean and J. D. Freeman, "Effects of ocean waves on airborne lidar imaging," Appl. Opt. **35**(18), 3261–3269 (1996).
17. C. Cox and W. Munk, "Measurement of the roughness of the sea surface from photographs of the sun's glitter," J. Opt. Soc. Am. **44**(11), 838–850 (1954).
18. C. Cox and W. Munk, "Statistics of the sea surface derived from sun glitter," J. Mar. Res. **13,** 198–227 (1954).
19. G. Tober, R. C. Anderson, and O. H. Shemdin, "Laser instrument for detecting water ripple slopes," Appl. Opt. **12,** 788–794 (1973).
20. C. S. Palm, R. C. Anderson, and A. M. Reece, "Laser probe for measuring 2-D wave slope spectra of ocean capillary waves," Appl. Opt. **16**(4), 1074–1081 (1977).
21. P. H. Y. Lee, J. D. Barter, K. L. Beach, C. L. Hindman, B. M. Lake, H. Rungaldier, J. C. Schatzman, J. C. Shelton, R. N. Wagner, A. B. Williams, R. W. Lee, and H. C. Yuan, "Recent advances in ocean-surface characterization by a scanning-laser slope gauge," in *Optics of the Air–Sea Interface: Theory and Measurement*, L. Estep, ed., Proc. SPIE **1749,** 234–244 (1993).
22. E. J. Bock and T. Hara, "Optical measurements of capillary-gravity wave spectra using a scanning laser slope gauge," J. Atmos. Ocean. Technol. **12**(2), 395–403 (1995).
23. B. A. Hughes, H. L. Grant, and R. W. Chappell, "A fast response surface-wave slope meter and measured wind-wave moments," Deep-Sea Res. **24,** 1211–1223 (1977).
24. S. Tang and O. H. Shemdin, "Measurement of high frequency waves using a wave follower," J. Geophys. Res. **88**(C14), 9832–9840 (1983).
25. S. P. Haimbach and J. Wu, "Field trials of an optical scanner for studying sea-surface fine structures," IEEE J. Ocean. Eng. **OE-10**(4), 451–453 (1985).
26. W. C. Keller, W. J. Plant, and D. E. Weissman, "The dependence of X band microwave sea return on atmospheric stability and sea state," J. Geophys. Res. **90**(C1), 1019–1029 (1985).
27. P. A. Hwang and O. H. Shemdin, "The dependence of sea surface slope on atmospheric stability and swell conditions," J. Geophys. Res. **93**(C11), 13903–13912 (1988).
28. J. Wu, "Effects of atmospheric stability on ocean ripples: a comparison between optical and microwave measurements," J. Geophys. Res. **96**(C4), 7265–7269 (1991).
29. J. A. Shaw and J. H. Churnside, "Fractal laser glints from the ocean surface," J. Opt. Soc. Am. A **14,** 1144–1150 (1997).
30. J. R. Apel, "An improved model of the ocean surface wave vector spectrum and its effects on radar backscatter," J. Geophys. Res. **99**(C8), 16269–16291 (1994).
31. J. Wu, "Slope and curvature distributions of wind-disturbed water surface," J. Opt. Soc. Am. **61**(7), 852–858 (1971).
32. S. D. Smith, "Coefficients for sea surface wind stress, heat flux, and wind profiles as a function of wind speed and temperature," J. Geophys. Res. **93**(C12), 15,467–15,472 (1988).
33. J. C. Kaimal and J. J. Finnigan, *Atmospheric Boundary Layer Flows: Their Structure and Measurement* (Oxford U. Press, Oxford, UK 1994), Ch. 1.
34. Y. G. Trokhimovski, E. R. Westwater, V. I. Irisov, and V. Y. Leuskiy, "A scanning 60 Ghz radiometer to measure air–sea temperature difference: recent results during COPE," in *IGARSS '96, Lincoln, NE, 27–31 May* (IEEE, New York, 1996), pp. 1672–1674.
35. C. W. Fairall, E. F. Bradley, J. S. Godfrey, G. A. Wick, J. B. Edson, and G. S. Young, "Cool-skin and warm-layer effects on sea surface temperature," J. Geophys. Res. **101**(C1), 1295–1308 (1996).
36. B. R. Frieden, *Probability, Statistical Optics, and Data Testing*, 2nd ed. (Springer–Verlag, New York, 1991), p. 56.
37. A. Papoulis, *Probability, Random Variables and Stochastic Processes*, 2nd. ed. (McGraw–Hill, New York, 1984), pp. 196–198.
38. W. H. Beyer, *CRC Standard Math Tables*, 27th ed. (CRC, Boca Raton, Fla., 1984), p. 496.
39. M. S. Longuet–Higgins, "The effect of non-linearities on statistical distributions in the theory of sea waves," J. Fluid Mech. **17,** 459–480 (1963).